

# Characterization of X-ray gas attenuator plasmas by optical emission and tunable laser absorption spectroscopies

Álvaro Martín Ortega,<sup>a\*</sup> Ana Lacoste,<sup>b</sup> Stéphane Béchu,<sup>b</sup> Alexandre Bès<sup>b</sup> and Nader Sadeghi<sup>c</sup>

Received 13 February 2017

Accepted 18 August 2017

Edited by S. Svensson, Uppsala University, Sweden

**Keywords:** gas attenuator; power absorption; optical emission spectroscopy; tunable laser absorption spectroscopy; plasma.

<sup>a</sup>ISDD, European Synchrotron Radiation Facility, 71 Avenue des Martyrs, 38043 Grenoble, France, <sup>b</sup>LPSC, Centre de Recherche Plasmas–Matériaux–Nanostructures, CNRS, UJF, INPG, 53 rue des Martyrs, 38026 Grenoble Cedex, France, and <sup>c</sup>LTM (UMR5129) and LIPhy (UMR5588), University Grenoble Alpes and CNRS, Grenoble, France.

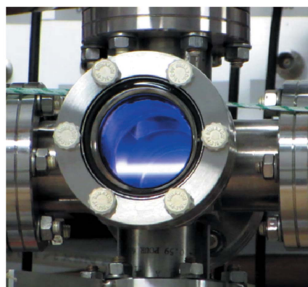
\*Correspondence e-mail: martinor@lpsc.in2p3.fr

X-ray gas attenuators are used in high-energy synchrotron beamlines as high-pass filters to reduce the incident power on downstream optical elements. The absorption of the X-ray beam ionizes and heats up the gas, creating plasma around the beam path and hence temperature and density gradients between the center and the walls of the attenuator vessel. The objective of this work is to demonstrate experimentally the generation of plasma by the X-ray beam and to investigate its spatial distribution by measuring some of its parameters, simultaneously with the X-ray power absorption. The gases used in this study were argon and krypton between 13 and 530 mbar. The distribution of the  $2p$  excited states of both gases was measured using optical emission spectroscopy, and the density of argon metastable atoms in the  $1s_5$  state was deduced using tunable laser absorption spectroscopy. The amount of power absorbed was measured using calorimetry and X-ray transmission. The results showed a plasma confined around the X-ray beam path, its size determined mainly by the spatial dimensions of the X-ray beam and not by the absorbed power or the gas pressure. In addition, the X-ray absorption showed a hot central region at a temperature varying between 400 and 1100 K, depending on the incident beam power and on the gas used. The results show that the plasma generated by the X-ray beam plays an essential role in the X-ray absorption. Therefore, plasma processes must be taken into account in the design and modeling of gas attenuators.

## 1. Introduction

One of the main limiting factors of the design and operation of X-ray synchrotron beamlines is the heat load on the first crystal of the silicon double-crystal monochromator (DCM) used in most synchrotron beamlines. The spectrum of the white beam, the X-ray beam emitted by the source, spans several keV of photon energy and can carry hundreds of watts per square millimeter (Biasci *et al.*, 2001). Most of this power is absorbed in the surface of the first crystal of the DCM, heating it up and inducing thermal deformations. These deformations destroy the necessary parallelism between the DCM surfaces and lead to a decrease in the transmitted photon flux. While active cooling systems based on liquid nitrogen and engineered cooling geometries are able to limit the deformations within a given range of heat loads, the deformations still appear if the heat load range is exceeded (Chumakov *et al.*, 2004; Zhang *et al.*, 2013).

A possible way to reduce the heat load in the DCM while maintaining a high photon flux is the use of attenuators. An attenuator is based on the Beer–Lambert law, according to



which the transmission of a photon beam passing through any material is determined by its absorption cross section,

$$I(E) = I_0(E) \exp[-\sigma(E)\rho z], \quad (1)$$

where  $\sigma(E)$  is the cross section at energy  $E$ ,  $\rho$  is the material density and  $z$  is the thickness of the material. Because of the energy dependence of  $\sigma$ , the low-energy photons are absorbed more efficiently than the high-energy ones; the choice of the material changes the absolute value of the cross section and the position of the absorption edges. However, the general trend remains. Therefore, a beamline operating at the high-energy end of the white-beam spectrum could use an attenuator placed between the white-beam source and the monochromator as a high-pass filter to reduce the flux of low-energy photons and the total incident power in the monochromator, all without significantly reducing the flux of high-energy photons transmitted afterwards by the monochromator. Traditionally, solid attenuators have been used because of their simplicity and well defined absorption properties, but they also have a maximum power absorption range given by the physical properties of the material used, and even below that limit they may experience damage during the operation cycles at which they are exposed. In addition, the absorption ratio is given by the material and thickness of the attenuator and cannot be changed. A newer alternative is gas attenuators, in which a vessel filled with a gas, usually argon or krypton, is placed in the beam path. The advantages are an adjustable absorption ratio by changing the vessel pressure and therefore density, the absence of a maximum operation temperature and a relaxed cooling requirement limited to the walls of the vessel. However, the heating of the gas following the power absorption, localized around the X-ray beam path, results in temperature and density gradients between the X-ray beam path and the walls of the attenuator vessel. As a consequence of the decrease in density, the absorption is reduced with respect to that expected from the initial density. This effect has already been observed in the gas attenuators used at the ESRF (European Synchrotron Radiation Facility) at the ID17 and ID15 beamlines (Requardt *et al.*, 2013; Hernández, 2010). Other gas attenuators, like that at the LCLS-I (Linear Coherent Light Source I) (Ryutov *et al.*, 2009), do not show this effect due to the small average power, but it is expected to appear in the upgraded LCLS-II (Feng *et al.*, 2016).

The absorption of the X-rays by the gas triggers a cascade of processes that must be taken into account to understand and predict the mentioned X-ray absorption. Initially, a fraction of the incident photons will be absorbed in the gas by Compton scattering, Rayleigh scattering and photoionization, the latter immediately followed by fluorescent and Auger decay. This results in the generation of a cascade of fast electrons that interact with the surrounding gas, exciting and ionizing atoms in their path as they lose their kinetic energy. The fast electrons also lose energy by elastic collisions, leading to the heating of the gas by the transfer of their kinetic energy from the electrons to the neutral species of the gas. As this process occurs, the electrons diffuse towards the walls of the

attenuator and, if their energy is low enough, recombine with ions in the volume of the gas. At the same time, the excited species generated in the process will decay emitting photons in the VUV and visible range. Further reactions, like the formation of the molecular ion  $\text{Ar}_2^+$  and its subsequent recombination (Petrov & Ferreira, 1999), act as a heat source, increasing the temperature of the gas and changing the local density.

If the number of free electrons is large enough, the diffusion and recombination of charged particles may play a relevant role in the power transfer. However, to our knowledge, previous experimental studies have considered only the overall X-ray absorption and temperature of the gas (Requardt *et al.*, 2013; Hernández, 2010) or the heat transfer following the power absorption (Feng *et al.*, 2016), but none of them have attempted to measure or model the ionization and recombination within the gas. The basic physics of the attenuator may be similar to that encountered in electron-beam (Aleksandrov *et al.*, 2005; Elson & Rokni, 1996) or extreme ultraviolet plasmas (Beckers *et al.*, 2016), although the specific differences with these sources, like the coupling between photon absorption and gas density or the pressure range of operation, call for a specific study on the attenuator plasma.

In this work we have measured the spatial distribution of the excited species of the gas by means of optical emission spectroscopy (OES) and tunable laser absorption spectroscopy (TLAS), together with the X-ray and power absorption. OES can provide the spatial distribution of excited atoms' densities in the  $\text{Ar}(2p)$  and  $\text{Kr}(2p)$  excited states while TLAS provides the density of  $\text{Ar}(1s_5)$  metastable atoms. The measurements of the X-ray power absorption and transmission were performed using calorimeters and a DCM. Additionally, Langmuir probe measurements were made to obtain a qualitative description of the electrical properties of the plasma, the pressure range being too high to apply standard probe theories. The objective is to demonstrate for the first time the generation of plasma by the X-ray beam in the gas attenuator and to determine its spatial distribution, temperature and excited-states concentration. The results relating gas temperature, power absorption and plasma properties could be used to validate theoretical models of X-ray gas attenuators, which so far are based only on power absorption and heat transfer by thermal conduction.

The rest of the paper is organized as follows: after this introduction, the general setup of the beamline used in this work is described in §2. In §3 the characterization methods and their implementation are described in detail. The results obtained for different cases and gas attenuators are presented, analyzed and discussed in §4, before the conclusions which are shown in the final section.

## 2. Beamline setup

The characterization of the X-ray generated plasma was performed on the ID06 beamline of the ESRF. The beamline setup used for both OES and TLAS is shown in Fig. 1. The

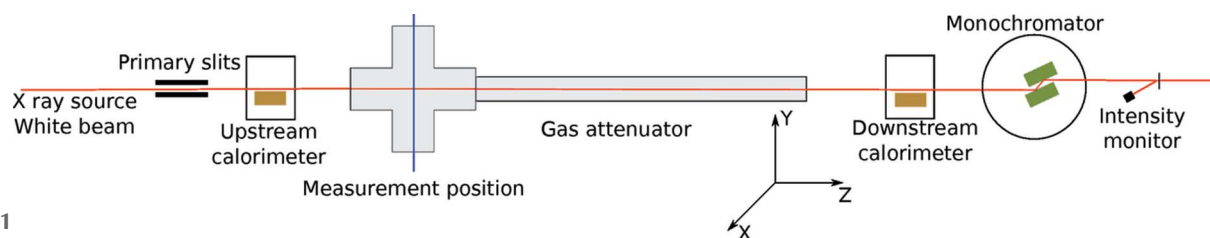


**Figure 1**  
Setup of the beamline for the optical and power absorption measurements.

X-ray source used was a U18 in-vacuum undulator (Chavanne *et al.*, 2011), with a tunable gap down to 6 mm. The smaller the gap, the higher the total power of the white beam; for instance, at 6 mm gap and 200 mA on the storage ring, the power emitted through a  $2\text{ mm} \times 2\text{ mm}$  aperture is 770 W. The aperture of the beam is controlled by the primary slits, placed at the entrance of the beamline, that can shape the beam to any size between 4 and 0.5 mm in the horizontal and vertical dimensions; both dimensions can be regulated separately. The gas attenuator is placed after the primary slits, flanked by two calorimeters immediately upstream and downstream to measure the beam power. Each calorimeter consists of a 2.17 kg copper block placed inside a vacuum chamber. The block can be moved in and out of the beam path, blocking the beam to measure its power or letting it pass to the next beamline component. Further downstream there is a Cinel DCM used to monochromatize the beam to any chosen energy between 2.5 and 100 keV. The monochromatic beam intensity is recorded by the beam intensity monitor, consisting of a metallic foil on the beam path and a photodiode detecting the scattered and fluorescence signal from the foil.

Two different gas attenuators were used in two experimental campaigns. The first attenuator, used for the OES measurements, had a gas chamber with a total length of 1.46 m divided into two segments. The first segment was a six-way cross of 18 mm diameter and 12.6 cm length, attached to the second segment consisting of a 1 m-long water-cooled double-wall cylinder of 12 mm inner diameter (Hernández, 2010). The second attenuator, used for the TLAS measurements, had a total length of 50.8 cm, with the gas chamber consisting of two six-way crosses of 18 mm diameter and 12.6 cm length separated by a cylinder of the same length and diameter. Both gas chambers were isolated from the vacuum of the beamline by two beryllium foils (0.5 mm thickness) placed inside a water-cooled copper frame. The gas pressure was recorded in both cases with a MKS 920B piezoelectric gauge, with a measurement range between 0.13 and 1333 mbar.

In addition to the optical diagnostics, the setup of which is described in detail in the next section, a cylindrical Langmuir probe was used in the first experimental campaign. It consisted of a 15 mm-long tungsten cylinder of 0.5 mm diameter, oriented parallel to the X-ray beam. The distance between the X-ray beam and the probe can be adjusted, as long as the probe does not touch the X-ray beam. If the probe touches the beam, the absorption of the X-rays will be so intense that the metal will melt in a few seconds. The probe was placed in the upper flange of the six-way cross used in the first attenuator. The typical pressure range of the attenuator prevents the use

of standard theories for the interpretation of the data from the probe, like the ABR or Laframboize ones (Allen *et al.*, 1957; Peterson & Talbot, 1970; Sudit & Woods, 1994; Chen, 2001), which require a non-collisional sheath around the probe (Rousseau *et al.*, 2005). However, the Langmuir probe measurements provide qualitative information on the plasma in two ways. First, the shape of the  $I(V)$  curve at high pressure will show whether there is plasma in the attenuator. Second, measurements at lower gas pressure (and therefore lower absorbed power), at which the standard theories are valid, will provide the value of some plasma parameters (electron temperature, plasma potential) that may be used to estimate their values at a higher pressure.

### 3. Diagnostics techniques

#### 3.1. X-ray power absorption

Two different techniques were applied to measure the X-ray power absorption: calorimetry and X-ray transmission at a selected energy. With the calorimeters we measure the incident  $P_{\text{in}}$  and transmitted  $P_{\text{tr}}$  power of the X-ray beam before and after the attenuator; the total absorbed power is calculated from the difference between these two values:  $P_{\text{abs}} = P_{\text{in}} - P_{\text{tr}}$ . The transmission at a single energy is obtained with the DCM and the intensity monitor, by measuring the transmitted intensity with  $[I(E)]$  and without gas  $[I_0(E)]$  at an energy peak  $E$  of the X-ray spectrum. Then, the average gas density along the beam path is calculated from these two values by inverting the Beer–Lambert law,

$$\rho = \frac{1}{\sigma(E)\Delta z} \log \left[ \frac{I_0(E)}{I(z, E)} \right], \quad (2)$$

where  $\sigma$  is the photon absorption cross section of the gas and  $\Delta z$  is the attenuator length. The values of the photon cross sections are well known; in our case we have used the values given by the NIST XCOM database (Saloman *et al.*, 1988). Both values (gas density and absorbed power) are related by the integral of the absorbed spectrum, which reads

$$P_{\text{abs}} = \int_E I_0(E) \{1 - \exp[-\sigma(E)\rho\Delta z]\} dE, \quad (3)$$

where  $I_0(E)$  is the incident spectrum and  $E$  is the photon energy. So, if the gas density and the incoming spectrum are known, the power absorbed can be calculated analytically applying equation (3); if the absorbed power and the incoming spectrum are known, the gas density can be calculated by inverting numerically the equation (3). In both cases knowl-

edge of the incoming spectrum is required; in this work we have obtained this from the synchrotron radiation simulation program *SRW* (Chubar & Elleaume, 1998). An instance of the simulated spectrum is shown in Fig. 2 together with the argon cross section. If the incident power measured by the calorimeters is different from the simulated one, the simulated spectrum is rescaled so that the total power becomes equal to the measured one. The rescaled spectrum is then used in the power absorption calculations. With these precautions taken, we should obtain the same results for gas density and absorbed power with both methods. In practice, only the X-ray transmission was measured for each experimental condition, with their results being verified by the calorimeters for a few cases. Because the measurement depends on having a sufficient absorption at the chosen energy, namely a peak of the incident X-ray spectra, the precision of the measurement decreases when there is little X-ray absorption. In our case, the measurements at lower pressure (and therefore lower power absorption) will have a smaller precision than those made at higher pressure. The results of the power absorption and gas density shown in the results section correspond to those obtained with X-ray transmission using the monochromator.

In addition to the gas density and absorbed power, we can also obtain an approximate value of the gas temperature along the X-ray beam path from the transmission measurements. The temperature of a gas is related to its density by the well known ideal gas law:  $p = nRT/V$ . In principle, one could apply this law to obtain the gas temperature from the gas density and pressure. In practice, due to the temperature and density gradients along the attenuator axis, the density obtained is only the average value along the X-ray beam path, so that we can only obtain an average of the *inverse* of the temperature,

$$\langle \rho \rangle = \left\langle \frac{pV}{RT_g} \right\rangle = \text{Cte} \left\langle \frac{1}{T_g} \right\rangle \simeq \text{Cte} \frac{1}{\langle T_g \rangle}, \quad (4)$$

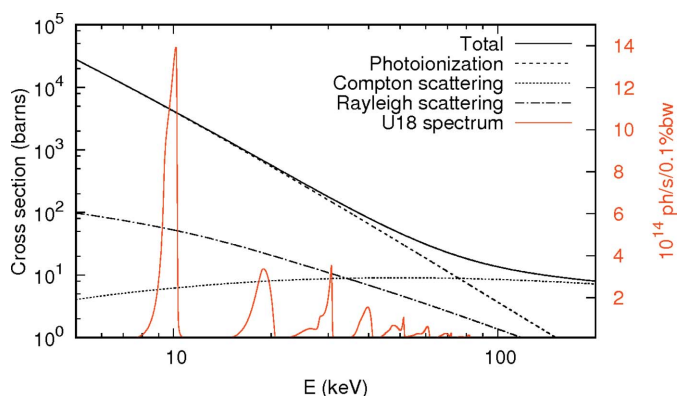


**Figure 2** X-ray spectra from a U18 undulator at 6 mm gap passing through an aperture of 2 mm × 2 mm at 30 m from the source, as calculated by *SRW* (Chubar & Elleaume, 1998) (right-hand Y scale), and photoabsorption cross section for argon, as given by the NIST XCOM database (Saloman *et al.*, 1988) (left-hand Y scale). Note that the higher total cross section is at low energies and is virtually equal to that of the photoionization.

where  $R$  is the ideal gas constant,  $p$  is the measured gas pressure,  $V$  is the volume over which we average (the volume crossed by the X-ray beam) and  $\text{Cte} = pV/R$  is the proportionality constant between the average density and the average inverse temperature. Calculating the gas temperature as  $\langle T_g \rangle \simeq \text{Cte}(1/\langle \rho \rangle)$  will result only in an approximation to the real average value, which nevertheless will give us a quantitative measure of the gas temperature along the X-ray beam path.

### 3.2. Optical emission spectroscopy

OES is a non-invasive technique, based on the measurement and analysis of the light emitted by the plasma, which can provide information about the population distribution in electronic, rotational or vibrational levels of atoms or molecules. Depending on the transition studied, different information can be obtained, like electron or gas temperature, electron density or heavy species concentration (Aragón & Aguilera, 2008; Belmonte *et al.*, 2015). In our case we will measure the spatial distribution of the plasma-induced light emission [as shown by Álvarez *et al.* (2002)]. It requires only a relatively simple setup consisting of a collimator to collect the light from a parallel line of sight and an optical fiber to take the collected light to the spectrometer. In addition, there is no fine alignment required: when a spatial scan is performed, the X-ray beam axis can be found as the symmetry axis of the spatial profile.

To perform the OES measurement, two flanges of the gas chamber were fit with fused silica windows, having a transmission higher than 95% in the 200–1000 nm spectral range. The light emitted by the plasma was collected by a 0.5 mm collimator and directed to an optical fiber (Fig. 3) placed at 10 cm from the collimator. The optical fiber was equipped with an autocollimating lens to ensure that only the light from a parallel line of sight was collected. The fiber was connected to an Avantes AVS-MC2000 spectrometer, which covers the 200 to 1000 nm spectral range, with a resolution of ~0.15 nm. The collimator and fiber assembly were connected to a motorized table, allowing for spatial scans on the vertical (for horizontal

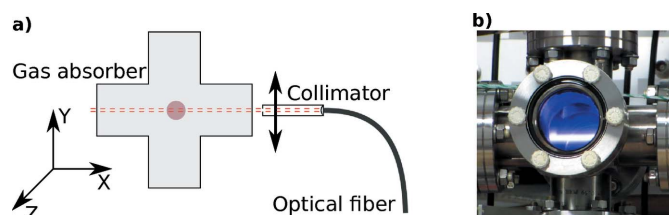


**Figure 3** (a) Schematic view of the optical setup for the OES measurements. The light is collected from the region between dotted lines by a collimator of 0.5 mm diameter, and focused onto the entrance face of an optical fiber, its other end connected to the spectrometer. The collimator is mounted on a movable table so that it is possible to scan along the Y direction. The X-ray beam crosses the attenuator in the Z direction and is represented by the central red circle. The whole setup is placed around the ‘measurement position’ shown in Fig. 1(b). (b) Image of the plasma in the gas attenuator as seen from the power facing the optical fiber.

**Table 1**

Argon and krypton lines used to perform the spatial scans using OES, corresponding to the most intense lines on the respective spectra.

Ar		Kr	
Wavelength (nm)	Transition	Wavelength (nm)	Transition
763.38	$2p_6 \rightarrow 1s_5$	758.60	$2p_5 \rightarrow 1s_4$
811.40	$2p_9 \rightarrow 1s_5$	760.09	$2p_6 \rightarrow 1s_5$
842.46	$2p_8 \rightarrow 1s_4$	811.24	$2p_9 \rightarrow 1s_5$
912.23	$2p_{10} \rightarrow 1s_5$	829.81	$2p_7 \rightarrow 1s_4$

line-of-sight) or horizontal (for vertical line-of-sight) directions, always perpendicular to the X-ray beam path.

The light emitted by the plasma on a particular emission line is given by the spontaneous emission equation

$$\varepsilon = \frac{1}{4\pi} n_2 A_{21}, \quad (5)$$

where  $A_{21}$  is the Einstein coefficient of the transition,  $n_2$  is the upper state density and  $\varepsilon$  is the emission intensity in photons  $s^{-1} \text{sterad}^{-1}$ . Accordingly, the spatial variations of the emission intensity will be proportional to those of the upper state density. However, the signal measured by the spectrometer is not the local emissivity but its projection along the line of sight of the collimator and optical fibre,

$$I(y) = \int_L \varepsilon(x, y) dx, \quad (6)$$

where  $L$  is the length of the line of sight. Assuming azimuthal symmetry of the emissivity,  $\varepsilon(x, y) = \varepsilon[(x^2 + y^2)^{1/2}] = \varepsilon(r)$ , its relation with the projected intensity can be expressed via the Abel transform,

$$I(y) = 2 \int_y^R \varepsilon(r) \frac{r}{(r^2 - y^2)^{1/2}} dr, \quad (7)$$

which can be inverted analytically

$$\varepsilon(r) = -\frac{1}{\pi} \int_r^R \frac{dI(y)}{dy} \frac{1}{(y^2 - r^2)^{1/2}} dy. \quad (8)$$

A number of methods exist to solve this inversion problem numerically (Sáinz *et al.*, 2006; Pretzier, 1991) to obtain the radial profile. The argon and krypton lines used in this work all belong to the  $2p-1s$  transitions (Table 1). They were found to have sufficient intensity in all of the experimental cases.

### 3.3. Tunable laser absorption spectroscopy

TLAS is a technique in which the wavelength of a laser with a narrow bandwidth ( $\sim$ MHz) is scanned around an atomic transition within a range of a few GHz while the transmitted signal is recorded by a photodiode. From the absorption profile one can obtain the density of atoms in the lower state of the line and the temperature of the gas. This method has been used in the study of a variety of plasma sources, like surfatron launchers (Hübner *et al.*, 2013; Carbone *et al.*, 2013), microwave discharges (Latrasse *et al.*, 2007), inductively coupled plasmas (de Regt *et al.*, 1996; Jonkers *et al.*, 1999) or

dielectric barrier discharges (Leiweke & Ganguly, 2013). In our case, we used a single laser source tuned to the  $1s_5 \rightarrow 2p_7$  transition of argon (772.38 nm) to deduce the radial distribution of the  $1s_5$  metastable atoms and the gas temperature; assuming thermal equilibrium, the temperature of the atoms in the metastable will be equal to that of the gas.

The laser setup for the TLAS measurements (Fig. 4) consisted of a diode laser (external cavity, Littrow configuration, Toptica) tuned to the 772.38 nm ( $3.88 \times 10^5$  GHz) transition of Ar, with a mode-hop-free mode scanning range of  $\sim 20$  GHz and a bandwidth of  $\sim 10$  MHz. The laser beam is split into three branches directed to a reference cell, to a Fabry–Perot interferometer and to the gas attenuator chamber. The reference cell consists of a low-pressure ( $\sim 1$  mbar) glow discharge and it is used to set the laser wavelength on the  $1s_5 \rightarrow 2p_7$  transition. The Fabry–Perot interferometer has a free spectral range of 0.375 GHz and it is used to calibrate the frequency shift of the laser, when scanning it. The beam directed to the attenuator is reflected on a mirror mounted on a motorized support and can scan the attenuator perpendicular to the X-ray beam, in the same way as for the OES. A diaphragm reduces the laser beam size to 0.5 mm in diameter. All three branches are terminated with photodiodes whose signals are simultaneously collected by a digital oscilloscope. To obtain the absorption signal, the background of the photodiodes  $I_{\text{back}}$  has to be subtracted from the laser signal  $I_{\text{off}}$  (X-ray off, no plasma and no absorption), and the light emitted from the plasma  $I_{\text{plasma}}$  has to be subtracted from the transmitted signal  $I_{\text{on}}$  (X-ray on, with plasma emission and absorption). The frequency-dependent shapes of those four acquisitions are shown in Fig. 5 when the

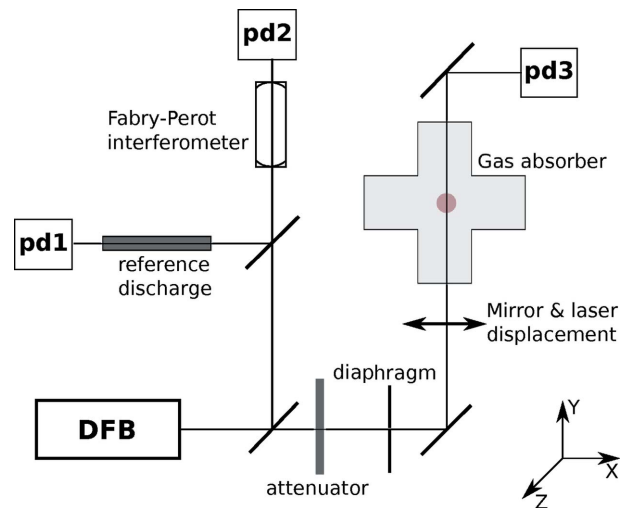


**Figure 4**

Schematic view of the optical setup for the TLAS measurements. The emitted laser (DFB) is split into three branches and directed to a Fabry–Perot spectrometer, to a reference cell discharge and to the gas attenuator. The branch directed to the gas attenuator is reduced in intensity and collimated to 0.5 mm diameter; it is also reflected by a movable mirror to obtain spatial scans of the laser absorption. All three branches are terminated by photodiodes (pd1, pd2 and pd3). The X-ray beam crosses the attenuator in the Z direction and is represented by the central red circle. The whole setup is placed around the ‘measurement position’ in Fig. 1.

laser frequency is scanned at  $3.88 \times 10^5$  GHz. The absorption signal is calculated as

$$K(\nu) = \log \left[ \frac{I_{\text{off}}(\nu) - I_{\text{back}}}{I_{\text{on}}(\nu) - I_{\text{plasma}}} \right] = \log \left[ \frac{I_0(\nu)}{I(\nu)} \right]. \quad (9)$$

The absorption of the laser beam is described by the Beer–Lambert equation,

$$\frac{dI(\nu, x)}{dx} = -k(\nu, x) I(\nu, x), \quad (10)$$

where  $I$  is the laser intensity in photons  $\text{s}^{-2} \text{m}^{-2}$ ,  $\nu$  is the laser frequency,  $x$  is the position along the laser beam and  $k$  is the local absorption coefficient. For an electronic transition like that measured here,  $k$  can be written as (Sadeghi, 2004)

$$k(\nu) = \frac{\lambda^2}{8\pi} \left[ n_l - \frac{g_l}{g_u} n_u \right] \frac{g_u}{g_l} A_{ul} \varphi(\nu). \quad (11)$$

Here,  $A_{ul}$  is the Einstein coefficient of the transition,  $\varphi(\nu)$  is the normalized line profile, and  $n_i$  and  $g_i$  ( $i = u$  for the upper and  $i = l$  for the lower states) are the  $i$  level density and degeneracy, respectively. The first and second terms inside the brackets account for the absorption and stimulated emission, respectively (Sadeghi, 2004). Under our plasma conditions,  $n_l$ , the density of  $1s_5$  metastable atoms, is expected to be much larger than  $n_u$  and therefore the stimulated emission can be neglected and the absorption coefficient simplified,

$$k(\nu) = \frac{\lambda^2}{8\pi} n_l(x) \frac{g_u}{g_l} A_{ul} \varphi(\nu). \quad (12)$$

Since  $n_l(x)$  is a function of position, the measured absorption for each frequency and beam position is the integral along the line of sight,

$$K(\nu, y) = \log \left[ \frac{I(\nu, 0, y)}{I(\nu, L, y)} \right] = \frac{\lambda^2}{8\pi} \frac{g_u}{g_l} A_{ul} \int_0^L n_l(x, y) \varphi(\nu) dx, \quad (13)$$

where  $L$  is the length of the plasma at the measured position. The integral over the line shapes gives

$$S(y) = \int_{-\infty}^{\infty} K(\nu, y) d\nu = \frac{\lambda^2}{8\pi} \frac{g_u}{g_l} A_{ul} \int_{-\infty}^{\infty} \int_0^L n_l(x, y) \varphi(\nu) dx d\nu. \quad (14)$$

The line-shape integral is equal to one, giving the simplified expression

$$S(y) = \frac{\lambda^2}{8\pi} \frac{g_u}{g_l} A_{ul} \int_0^L n_l(x, y) dx = \frac{1}{C} \int_0^L n_l(x, y) dx, \quad (15)$$

which relates the integral value over the line shape at each position to the projected metastable density along the line of sight, with the constant  $C$  depending on the specific transition [ $1.36 \times 10^7 \text{ s m}^{-2}$  for the studied  $1s_5 \rightarrow 2p_7$  transition (Hübner *et al.*, 2013)]. If, as in the OES case, one assumes that the metastable density  $n_l(x, y)$  has azimuthal symmetry, it is possible to apply equations (7) and (8) to obtain its value as a function of the radial position  $n_l(r)$ .

The line shape of the absorption signal is determined by several broadening mechanisms: natural, Stark, Doppler and van der Waals broadening. Following Palomares *et al.* (2010) and Konjevic *et al.* (2002), the natural absorption broadening contributes only around 6 MHz, so it can be neglected here. The full width at half-maximum (FWHM) of the Stark broadening of the argon 772.38 nm line is given by Konjevic *et al.* (2002),

$$\Delta\nu_S [\text{GHz}] = 3.4 \times 10^{-16} n_e [\text{cm}^{-3}], \quad (16)$$

which can become important for electron densities higher than  $10^{14} \text{ cm}^{-3}$ . The Doppler broadening, due to the thermal movement of the atoms, has a Gaussian profile with a FWHM of

$$\Delta\nu_D [\text{Hz}] = 7.6 \times 10^{-7} \nu (T_g/M)^{1/2}, \quad (17)$$

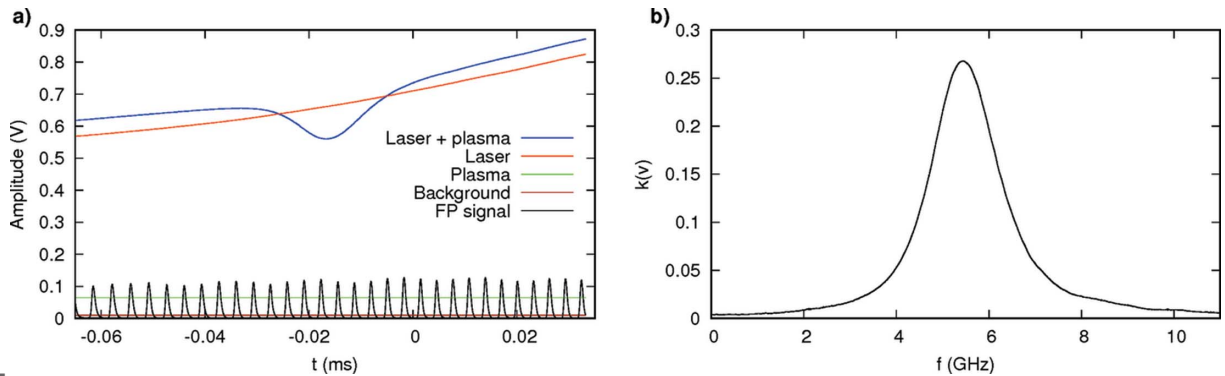


**Figure 5** (a) Intensity of recorded signals for obtaining the absorption profile as a function of time (while the laser frequency is continuously shifted): background, plasma signal (both with laser off), laser (laser on, X-ray off) and absorption (laser on, X-ray on). The Fabry–Pérot signal (FP) provides the frequency shift during the laser scan. (b) Absorption spectrum after transformation to the frequency scale.

where  $T_g$  is in K,  $M$  is the atomic mass in a.m.u. and  $\nu$  is the photon frequency in Hz. This mechanism becomes dominant at low electron density and low (<10 mbar) pressure. The remaining contribution is the van der Waals broadening due to collisions of the metastable (absorber) atoms with other neutral atoms. It has a Lorentzian profile with a FWHM of (Hübner *et al.*, 2013)

$$\Delta\nu_{\text{vdW}} [\text{Hz}] = Kp(300/T_g)^{0.7}, \quad (18)$$

where the temperature  $T_g$  is in Kelvin and  $p$  is the pressure in mbar.  $K$  is a transition-dependent constant, which for the measured transition (Hübner *et al.*, 2013) has a value of 1.6 ×

10<sup>7</sup>. So, at  $p \simeq 100$  mbar, assuming  $n_e \leq 10^{14} \text{ cm}^{-3}$ , the natural and Stark broadenings can be neglected and the absorption profile has a Voigt shape (Belostotskiy *et al.*, 2010), with its Gaussian component being  $\Delta\nu_D$  and its Lorentzian component equal to  $\Delta\nu_{\text{vdW}}$ .

## 4. Results and discussion

### 4.1. Power absorption

The results of the power absorption, calculated from the X-ray transmission measurements [equations (2) and (3) in §3.1], are shown in Figs. 6(a) and 6(b), plotted *versus* the gas pressure. The data from the two experimental campaigns are

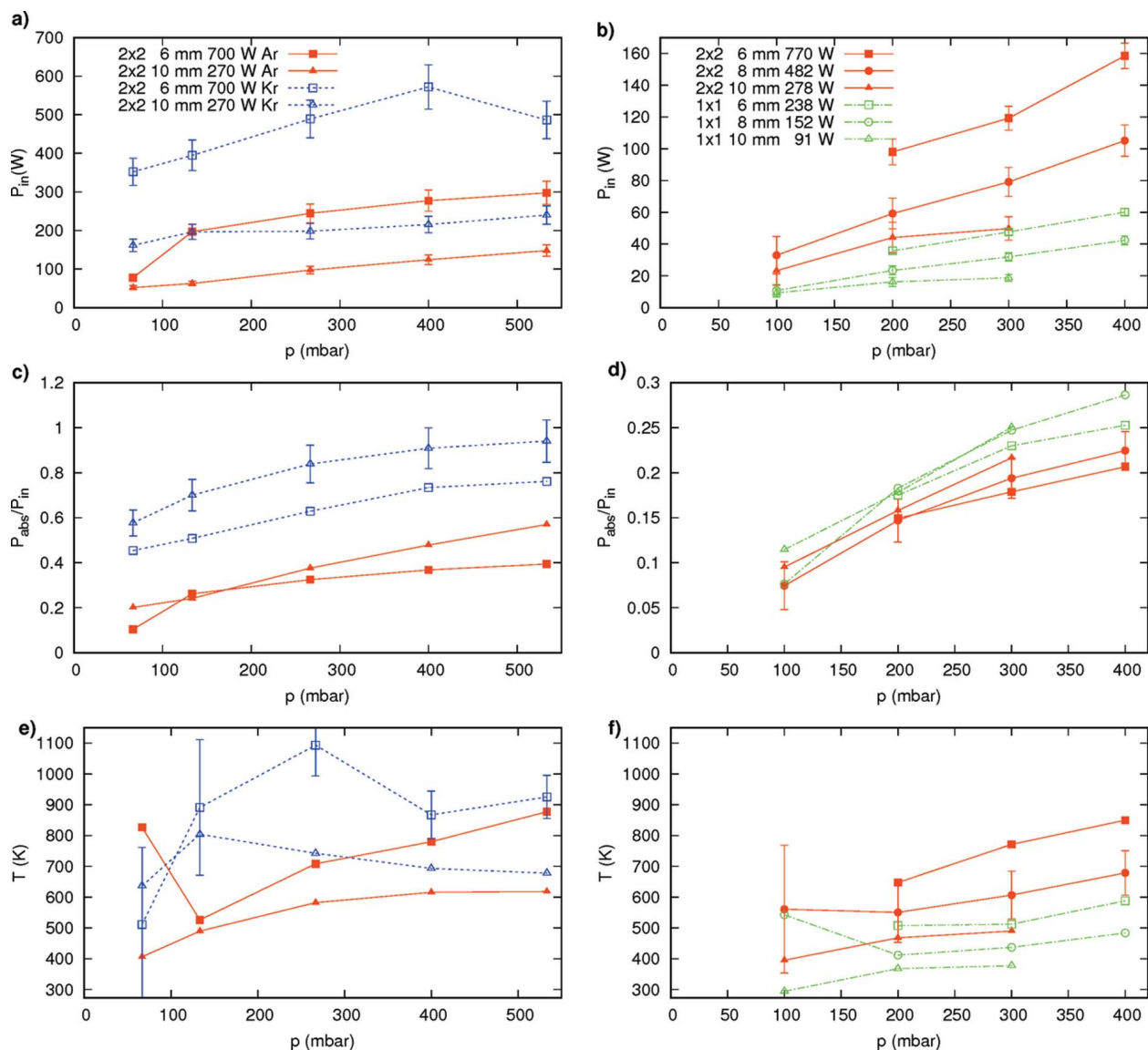


**Figure 6** Results obtained from the X-ray absorption measurements: total absorbed power (a and b), fraction of absorbed power (c and d) and average gas temperature (e and f) as a function of gas pressure. The results for each experimental campaign are shown separately: parts (a), (c) and (e) correspond to the OES setup (1.46 m length of attenuator) where argon and krypton were used, and parts (b), (d) and (f) correspond to the TLAS setup (50.8 m length of attenuator) where only argon was used. The keys shown in the two top plots of each column indicate the X-ray beam size, undulator gap (related to the spectrum), X-ray beam power and, for plots (a), (c) and (e), the gas used.

shown separately to simplify their interpretation. Fig. 6(a) shows the results for the OES setup, in which both argon and krypton were used, and where the attenuator length was 1.46 m. Fig. 6(b) shows the results for the TLAS setup, using only argon and where the attenuator length was 0.5 m. The difference in the scale of the absorbed power results from the longer attenuator on the OES setup than in the TLAS one. Apart from this, the first observation that can be made is the general increase of the absorption with the gas pressure, for each given set of X-ray beam properties (spectrum, size and power). This is something expected, since an increase in pressure means an increase in density and in, according to the Beer–Lambert law, the X-ray absorption rate. Also, in Fig. 6(a) we can see that, owing to its higher cross section, krypton absorbs more than argon. The change in the trend observed for krypton at 550 mbar and 770 W of (nominal) input power is due to the variations on the actual input power. The input power may be reduced to 80% of the nominal value because of the decrease in the synchrotron current, which is refilled periodically. To account for the effect of the changes of the input power, the *fraction* of the absorbed power is shown in Figs. 6(c) and 6(d) for the first and second experimental campaigns, respectively. The fraction of the absorbed power increases with the gas pressure, without exceptions. Another observation is that the absorbed fraction is higher for lower input power, although the total absorbed power is still lower. The reason for this is that, as the input power increases, so does the heating of the gas. This results in an increase in the temperature and a decrease in the density and in the absorption ratio.

The corresponding temperatures [Figs. 6(e) and 6(f)], calculated from equation (4), do not follow a clear trend, having cases where the temperature increases with the pressure and cases where it decreases. There are two possible reasons for this behaviour. First, as we increase the pressure, both the heating and the cooling increase, and the balance between them is complex enough to not follow a constant trend. For example, an increase in pressure could increase the heat transfer by convection. Second, the temperatures obtained are not a local values but an average one, and therefore do not reveal anything about the local values or the axial temperature profile along the beam path, which could impact the average temperature in different ways. In addition, the impact of the experimental error is much larger in the calculation of the temperature than in the power absorption: an approximately constant error of 10 W in the power absorption becomes an error of 50 K at 400 mbar and of more than 100 K at 100 mbar. This may explain the deviation from the trend of the points at 100 mbar in Fig. 6(f). However, it is unlikely to cause the lack of a trend in Fig. 6(e), where the attenuator is longer and the absorption signal stronger. Rather, this lack of a trend indicates the changes in the balance of heating and cooling processes and the error in neglecting the temperature gradients across the attenuator length. Precisely because of the shorter length of the attenuator of the second campaign (Fig. 6f), the temperatures obtained in that case should be more representative of

the average temperature than those of the first campaign (Fig. 6e).

#### 4.2. Langmuir probe

Langmuir probe measurements were performed at gas pressures between 0.67 and 533 mbar for krypton and between 1.33 and 533 mbar for argon, at positions between 3 and 15 mm from the X-ray beam axis (coincident with the attenuator axis). At lower pressures the X-ray absorption and subsequent gas ionization was so low that the current collected by the probe was too weak to be analysed. A sample of the curves obtained is shown in Fig. 7 for different pressures of argon. The fact that gas acts as a conductor and not as an insulator is a first indicator of the presence of plasma. The curves show a standard  $I(V)$  characteristic: a small ionic current for negative polarity of the probe and a strong electronic current for the positive polarity. The curves are plotted with respect to the ground potential and not to the plasma potential: there is no externally applied electric field, and therefore the plasma potential is only a few volts above the ground potential. The amplitude of the electronic branch increases with the pressure, indicating a higher electron density which is induced by the higher X-ray power absorption.

Besides this qualitative analysis, we have performed a detailed analysis of the curves obtained at lower pressure (1.33 mbar) following the Laframboise theory (Sudit & Woods, 1994). Fig. 8 presents the electron density and the electron temperature as a function of radial position (the starting position corresponds to 5 mm). The electron temperature is below 1 eV and decreases as the distance from the X-ray beam increases. The electron density, of the order of  $3 \times 10^{14} \text{ m}^{-3}$ , also decreases far from the X-ray beam. The corresponding Debye (screening) length, given by  $\lambda_D = [\epsilon_0 k_B T_e / (n_e q_e^2)]^{1/2}$ , is  $\sim 0.43 \text{ mm}$  in all of the positions considered. Hence, the Debye length being smaller than the attenuator radius (12 mm) demonstrates that the gas can be considered a plasma and that the free charges created behave collectively. The plasma potential measured by the probe follows the same trend as the electron temperature and

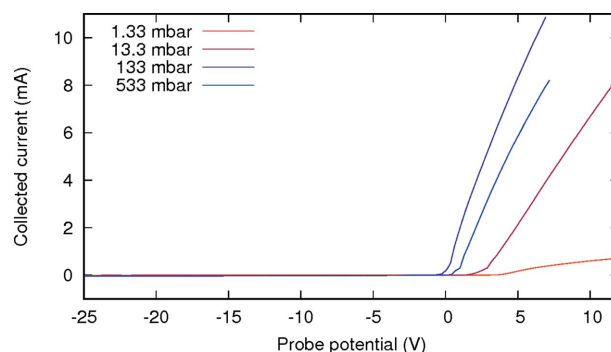


**Figure 7** Current–voltage curves taken with the Langmuir probe at 10 mm from the attenuator axis, with an X-ray beam of 2 mm × 2 mm size and 6 mm gap in the U18 undulator ( $\sim 770 \text{ W}$  input power), for different pressures of argon.

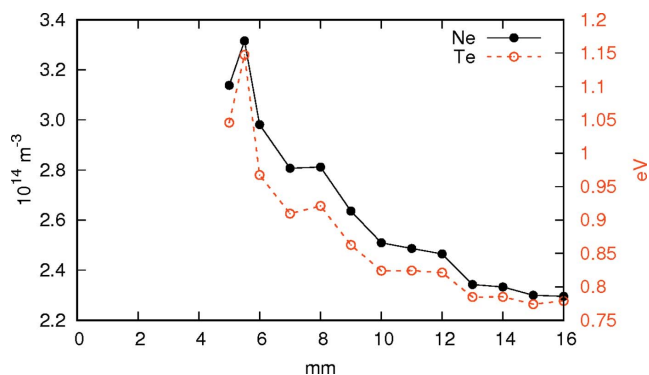


**Figure 8**  
Electron density (continuous line, left-hand Y scale) and temperature (dotted line, right-hand Y scale) measured by the Langmuir probe as a function of distance to the X-ray beam axis, for a gas pressure of 1.33 mbar of argon and an X-ray beam of 2 mm × 2 mm and 6 mm gap in the undulator.

density, with values of  $\sim 5.1$  V and  $\sim 4.7$  V at 4.5 mm and 16 mm, respectively, from the attenuator’s axis. The power absorption at this gas pressure (1.33 mbar) was too low to be measured by either the calorimeter or the monochromator. However, assuming that the temperature of the gas remained at 300 K, one can calculate the total power absorption from

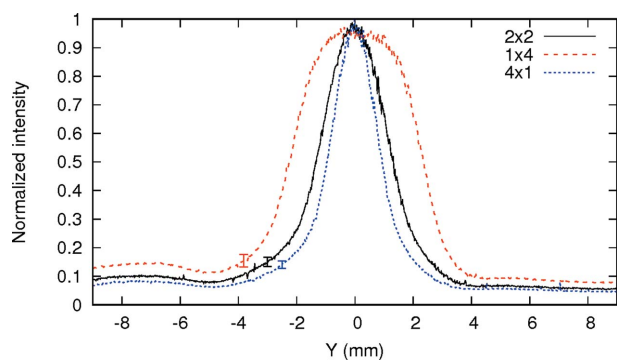


**Figure 9**  
Scan of the OES signal intensity along the vertical direction ( $Y$ ), for 400 mbar argon, 6 mm gap in the undulator and a variable beam size (shown in the legend). The channel intensities have been normalized to its maximum value and averaged to simplify the comparison.

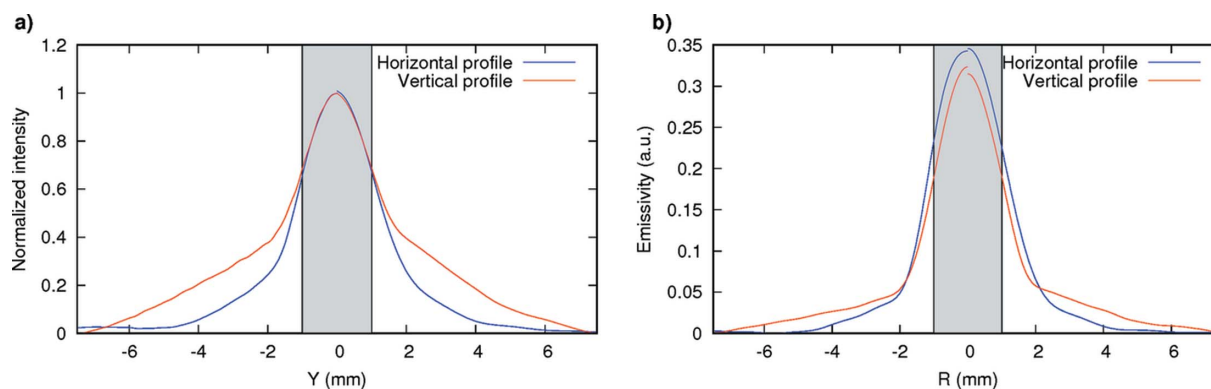


**Figure 10**  
Measured projection ( $a$ ) and reconstructed emissivity ( $b$ ) as a function of the lateral position ( $Y$ ) and radial position ( $R$ ), respectively, for scans in the horizontal and vertical direction. Gas pressure: 400 mbar argon; undulator gap: 10 mm; beam size: 2 mm × 2 mm. The signal of the four different channels has been normalized to the same maximum value and averaged. The gray area represents the area illuminated by the X-ray beam. Note that in this region both horizontal and vertical profiles match.

the corresponding gas density; this is equal to 4.1 W (over 770 W of incident power). At higher gas pressure, the power absorption is higher, and so must be the amount of ionization in the gas. One could expect then that in these cases plasma is also formed in the attenuator, the specific electron density depending not only on the direct ionization but also on the balance between diffusion, recombination and ionization.

To obtain reliable values of the electron density, it would be possible to use alternative methods adapted to this pressure range, like microwave interferometry (Deline *et al.*, 2007), Thompson scattering (Palomares *et al.*, 2010) or microwave cavity resonance spectroscopy (Beckers *et al.*, 2016).

### 4.3. OES results

The main objective of the OES scans is to determine the radial profile of the plasma generated by the X-ray beam, assuming it has the same profile as that of the excited atoms in the  $2p$  states of the gas. The first step is to verify whether the optical system can capture variations on the size of the active plasma region. A set of three scans with asymmetric beam profiles ( $x/y = 4/1, 2/2$  and  $1/4$  mm) were recorded with argon at 400 mbar. For each scan, the four spectral lines listed in Table 1 were recorded simultaneously. The results are shown in Fig. 9, in which we can appreciate that the spatial profile becomes narrower when we reduce the beam size. The FWHM of the profiles in the  $Y$  direction (see Fig. 3) are 1.9, 2.6 and 4.6 mm for the 1, 2 and 4 mm of beam size along the  $Y$  axis, respectively. This demonstrates that the setup has enough spatial resolution to capture the variations in the plasma size, and that the active plasma region is effectively confined around the X-ray beam.

The next step is to study the azimuthal symmetry of the plasma region with a square-shaped X-ray beam. To this end, two scans, one horizontal and one vertical, were taken using a 2 mm × 2 mm beam and a gas pressure of 400 mbar argon, with a gap in the undulator of 10 mm ( $\sim 270$  W input power). These scans are shown in Fig. 10, together with their respective emissivities calculated by Abel transform. Both scans have a similar profile around the center, with more intense wings in

the horizontal than in the vertical. However, this difference might be the effect of a difference in the stray light, due to a difference in the cross section of the attenuator. In the horizontal scan, it was a cylinder of 12 mm radius with a flange only in the vertical side, while in the vertical scan it was a 18 mm-radius six-way cross section with flanges in both sides. The difference in the stray light will be less important around the center, where the light comes mainly from the plasma itself and where both scans and their respective Abel transforms coincide. Therefore, we can conclude that the plasma shows a similar profile in the horizontal and vertical directions. While this alone is not enough to demonstrate the azimuthal symmetry (and the validity of the Abel transform), it can be justified by the diffusion of electrons and other particles. Although the diffusion is small enough to keep the plasma confined around the X-ray beam, even a small amount could smooth the corners of a square-shaped beam, making the approximation of azimuthal symmetry reasonable. In addition, the results of the Abel transform will be used to study only the overall size of the plasma region, not the details of its distribution.

Now we can compare the size of the plasma region as a function of the gas pressure, type and X-ray beam properties (size, power and spectrum). Fig. 11 shows the FWHM of the plasma region for argon (66–550 mbar) and krypton (13–550 mbar) for two X-ray beam configurations each. It was possible to make measurements at lower pressure with krypton than argon because of its higher X-ray absorption and light emission; at lower pressure there is less absorption and therefore not enough signal. We can see that between 50 and 550 mbar the size of the plasma region does not change with pressure, which means that diffusion is already slow enough to keep the plasma confined around the X-ray beam. The changes in the FWHM with pressure are of the same magnitude as the estimated error of its value. Only the size of the X-ray beam determines the size of the plasma. One must decrease further the pressure of the gas (point at 13 mbar krypton) for the diffusion to increase enough to enlarge the size of the plasma region.

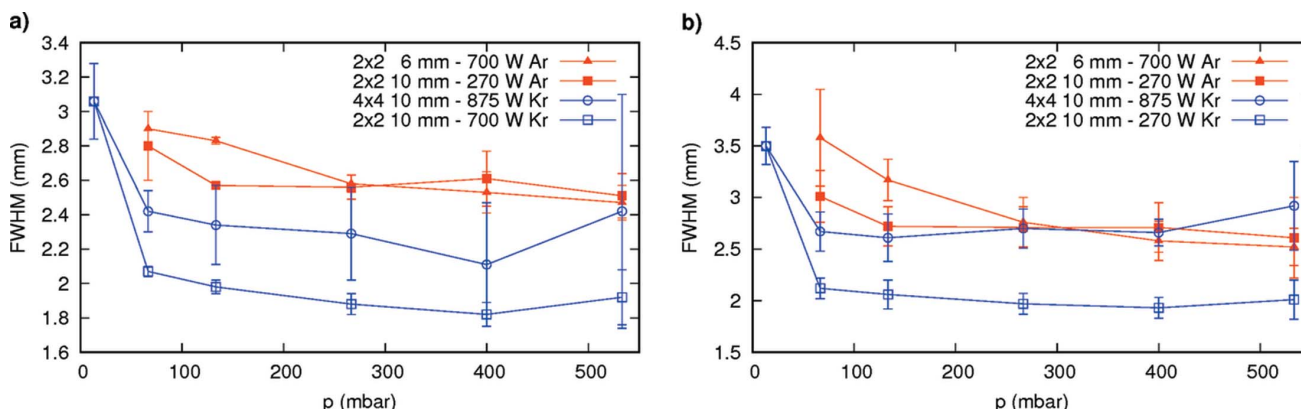
We can also compare, still in Fig. 11, the plasma size as a function of the X-ray power and spectrum. For argon, the two

measurement series were made with the same beam size and different gap (therefore different power), resulting in almost identical active region sizes. Only when changing the beam size, as was done in the two series with krypton, does the size of the active region change. As for the difference between different gases, when using krypton the active region is smaller than for argon, for the same gas pressure and beam size. This is because krypton has a larger electron-impact cross section [ $\sim 1.5$  times that of argon for ionization and excitation collisions (LXCat, 2015)], resulting in a more effective slow-down of energetic electrons issued from photoionization and Auger decay, and a decrease of the region where the ions and excited species are produced.

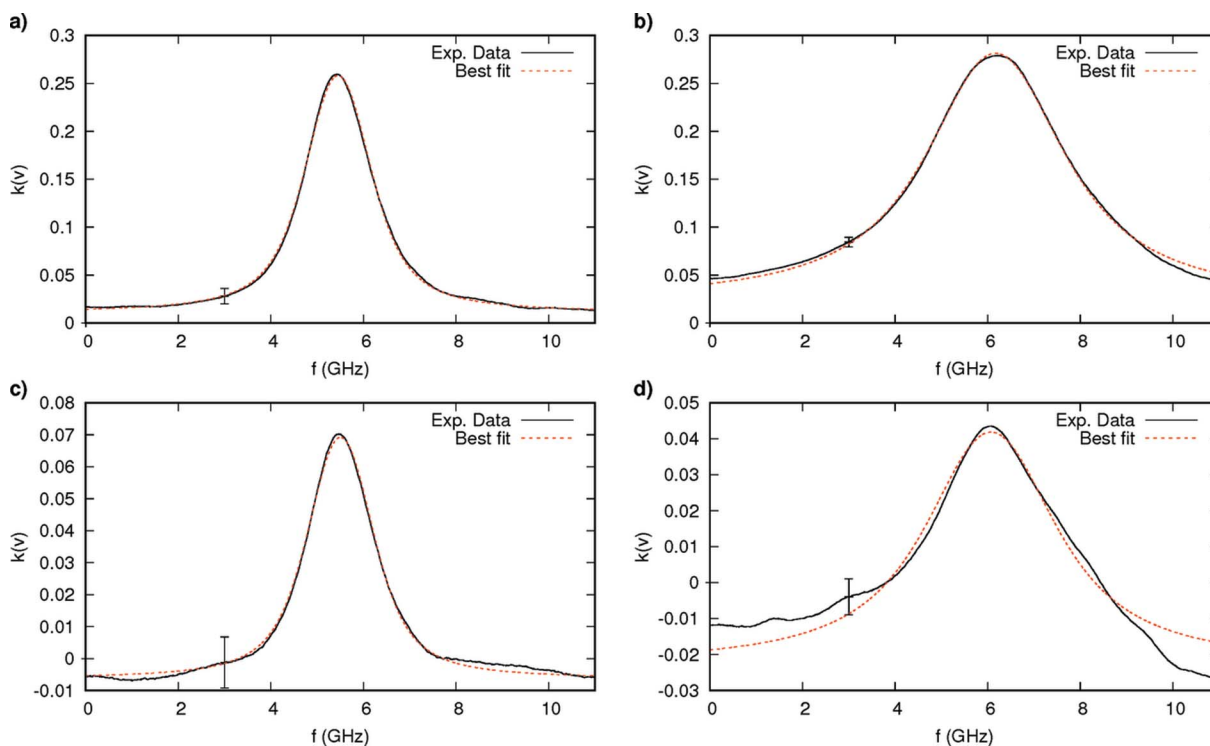
#### 4.4. TLAS results

For the TLAS, the experimental conditions were: argon pressures of 100, 200, 300 and 400 mbar; 6, 8 and 10 mm gap in the undulator; beam sizes of 1 mm  $\times$  1 mm and 2 mm  $\times$  2 mm. For all gas pressures and X-ray beam properties the absorption measurements were performed at steps of 0.5 mm around the X-ray beam axis and with larger steps (1 mm and 2 mm) in the regions where the absorption signal became weaker. The transmission (laser on, X-ray off) and absorption (laser on, X-ray on) measurements were taken for every position, while the plasma and background signals were constant for all the points and were taken only once for each operating condition. The absorption signal is then calculated using equation (9), and then fitted to a Voigt function using the Gaussian and Lorentzian components in equations (17) and (18), with the gas temperature, assumed homogeneous inside the diagnostic volume, as the free parameter.

Fig. 12 shows the fits for 100 and 300 mbar pressure at the center and at 4.5 mm from the X-ray beam axis, determined as the position at which the metastable state density reaches its maximum value. The signal becomes much smaller at this distance from the center, so that the noise becomes more important and the quality of the fit decreases. This can also be noted in Fig. 13, where the metastable density obtained from equation (15) and the gas temperature obtained from the fit are shown. The metastable density is higher at the center and

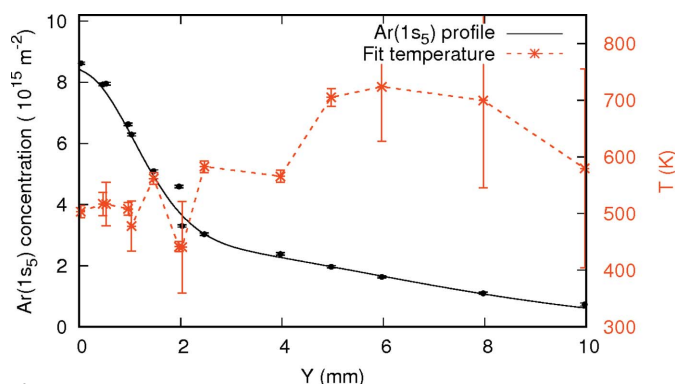


**Figure 11** FWHM of the projected profile (a) and the reconstructed emissivity (b) as a function of the pressure for different gases and beam parameters. The plotted value is the average of the FWHM from each of the four channels used.


**Figure 12**

Absorption signal at the center for 100 mbar (a) and 300 mbar (b) and at 4.5 mm from the X-ray beam axis at the same pressures (c and d) as a function of the frequency shift, together with the best fit for each case. In all of the cases the undulator gap was 6 mm, the beam size  $2 \text{ mm} \times 2 \text{ mm}$  and the gas used argon (Ar  $1s_5$  metastable state). The origin of the frequency was chosen as the start of the frequency scan.

decreases monotonically towards the wall of the attenuator, as could be expected. However, the temperature has nonphysical oscillations and a much larger statistical error in the region where the metastable density is low; this is due to a poor fit arising from weak and noisy absorption signals. As a consequence, the only meaningful temperature results are those obtained around the X-ray beam axis, where the fit quality is better and the relative noise lower. This means that, while we can compare the complete metastable density profile obtained


**Figure 13**

Metastable ( $1s_5$ ) density projection (continuous line) and fit temperature (dotted line) of the absorption profile as a function of the measurement position for the case of 100 mbar of argon, 6 mm-gap undulator and  $2 \text{ mm} \times 2 \text{ mm}$  X-ray beam size. The density profiled was obtained using a smoothing spline between the points. The oscillations in the fit temperature are due to the small and noisy absorption signal far from the center, resulting in large noise and a poor fit.

from the TLAS, only a central temperature can be obtained from it.

The central temperature is taken as the average of the five central points, and the error as the difference between the maximum and the minimum temperature within those points. The results calculated this way are shown in Fig. 14 together with the temperatures obtained from the X-ray absorption measurements. We can see that in general the TLAS temperatures are lower than those obtained from the X-ray absorption. While the difference between both techniques may be equal or smaller than the estimated error, the fact that the temperature is systematically lower in the TLAS measurement points to some systematic error. There are several factors that might affect the fit of the Ar( $1s_5$ ) absorption profile, like uncertainties in the van der Waals broadening coefficient or a non-negligible Stark broadening. A contribution of the latter to the line broadening would lead to a corresponding smaller van der Waals broadening, when the total Lorentzian component remains constant, and an increase of the resulting gas temperature. However, to perform this procedure, knowledge of the electron density and temperature is required.

To obtain the radial profile of the metastable density, we need first to verify whether the system has enough spatial resolution. As in the OES, we measured the absorption profile for two beam sizes,  $1 \text{ mm} \times 1 \text{ mm}$  and  $2 \text{ mm} \times 2 \text{ mm}$  for identical gas pressure (100 mbar) and undulator gap (6 mm). The results of the normalized measured projection and corresponding metastable density profile are shown in Fig. 15.

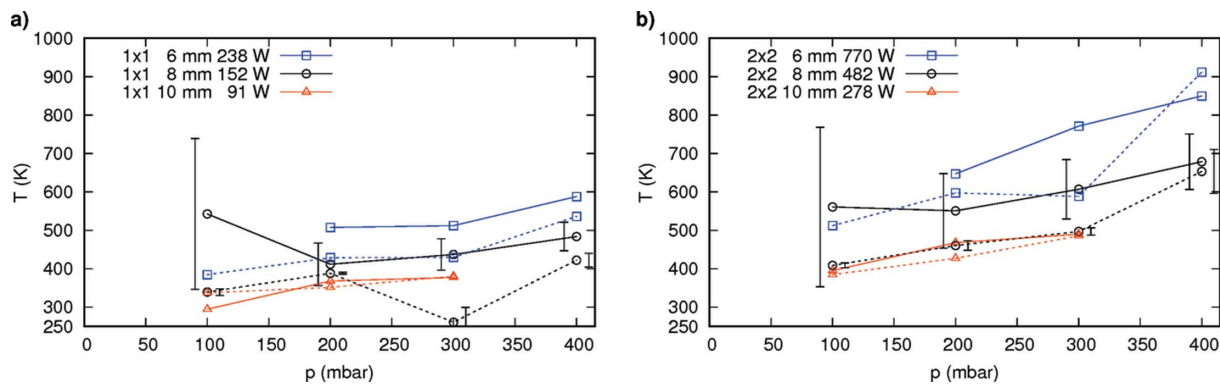


**Figure 14** Comparison of the gas (argon) temperatures obtained by X-ray transmission (full lines) and those obtained from the average of the three central temperatures on each scan by TLAS (dotted lines), with beam sizes of 1 mm × 1 mm (a) and 2 mm × 2 mm (b). The separation has been made for clarity on the plots. The error bar to the left of the point corresponds to the error in the X-ray transmission measurement; the error bar to the right corresponds to the error in the TLAS. Only one error bar is shown for each pressure.

The two beam sizes yield very different profiles, which means that the system has sufficient spatial resolution to resolve the difference. In comparison, the profiles obtained for the same beam properties and different gas pressure (Fig. 16) are almost identical within the X-ray beam region, with the higher-pressure case showing a more rapid drop of the metastable density far from that region. A probable reason for this is that, as the particle density increases, the metastable mobility decreases

and the quenching by three-body reaction involving two ground-state atoms increases (Belostotskiy *et al.*, 2011), with the result that the metastable atoms decay before reaching far from the central region.

As in the OES case, the FWHM of the metastable density and projected profiles do not change significantly with pressure or beam power, but only with beam size (Fig. 17). The reason for this is the same as before: even in the lower-pres-

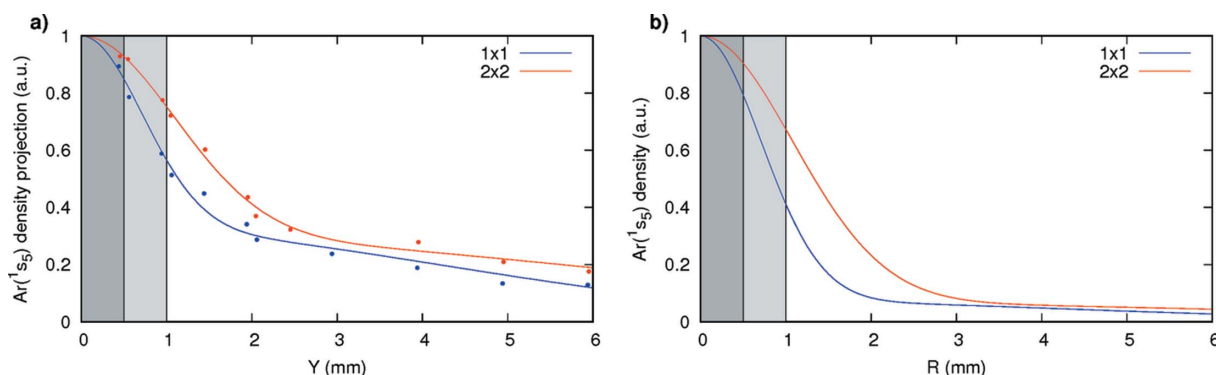


**Figure 15** Metastable projection normalized profile as a function of the lateral position (a) and reconstructed metastable density profile as a function of the radial coordinate (b) for beam sizes of 1 mm × 1 mm and 2 mm × 2 mm and 6 mm undulator gap. The gas pressure was 100 mbar in both cases. The gray areas indicate the size of the X-ray beam: dark gray for 1 mm × 1 mm and light gray for 2 mm × 2 mm.

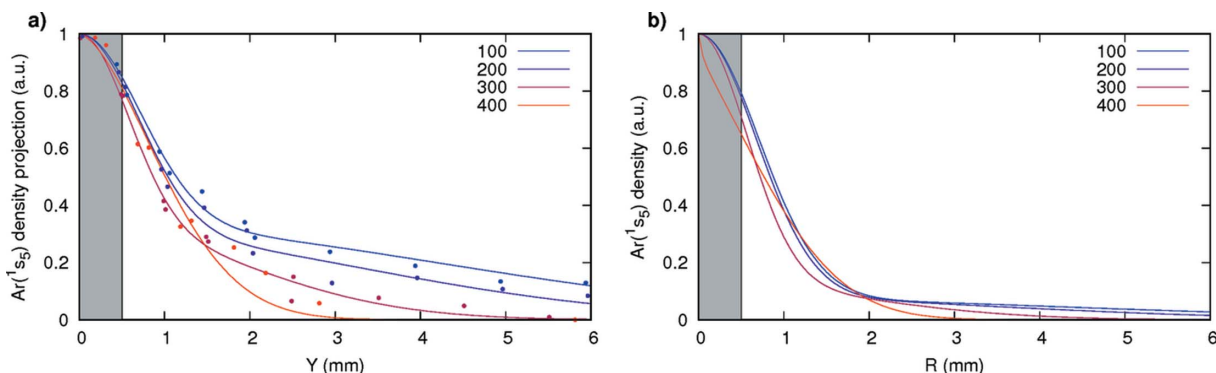


**Figure 16** Metastable (Ar 1s<sub>5</sub>) projection normalized profile as a function of the lateral position (a) and reconstructed metastable density profile as a function of the radial coordinate (b) for a beam size of 1 mm × 1 mm, 6 mm undulator gap and different argon pressures. The gray area indicates the size of the X-ray beam.

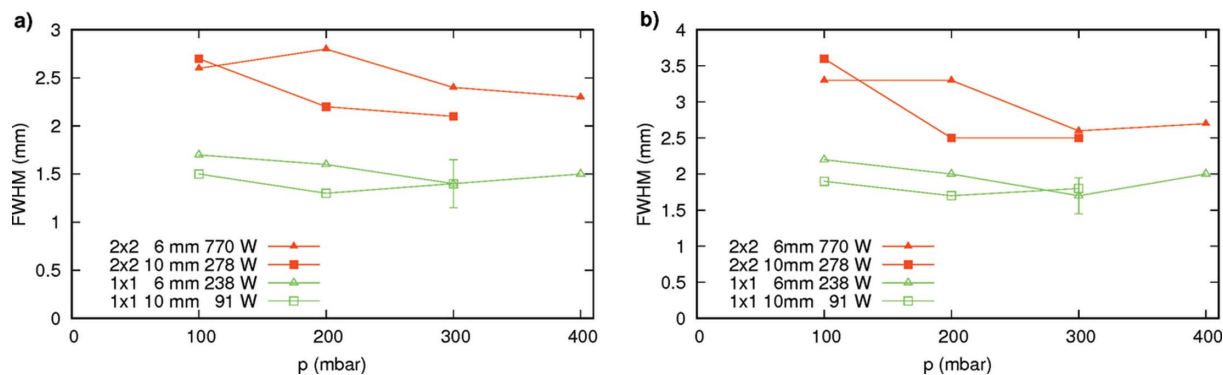


Figure 17

FWHM of the Ar( $1s_5$ ) projection profile (a) and density profile (b) as a function of the argon pressure, for different beam sizes and incident spectra. The error was estimated as constant and equal to half the distance between points in the spatial scan (0.5 mm).

sure case, the gas density is high enough to prevent fast electrons diffusing far away from the X-ray beam and to prevent metastable atoms diffusing within their lifetime from the place where they are born. This was true in the OES case where the observed emission was from  $2p$  states, which decay rapidly to  $1s$  states. In the case of the monitored  $1s_5$  metastable atoms, they are destroyed by electron-impact transfer to the  $1s_4$  resonant level (Carbone *et al.*, 2015) and by three-body collisions with ground-state Ar atoms (Belostotskiy *et al.*, 2011). The confinement of these long-lived metastable atoms indicates that their diffusion will not be a significant mechanism of the energy transfer towards the walls of the attenuator. The power transferred to the Ar( $1s_5$ ) state will mainly be released *via* the radiative decay of either the Ar( $1s_4$ ) resonant state (at 105 nm) or the Ar $_2^*$  excimer ( $\sim 126$  nm) formed by three-body collisions. Both of these types of vacuum ultraviolet radiation end on the attenuator walls, heating them.

## 5. Conclusions

In this work we have performed, to our knowledge for the first time, the diagnosis of the plasma formed on an X-ray gas attenuator. Plasma generation is confirmed by Langmuir probe measurements at the plasma edge, that show an electron density of the order of  $3 \times 10^8 \text{ cm}^{-3}$  and a plasma potential of around 5 V. These results were obtained for a relatively low pressure (1.33 mbar) corresponding to low absorbed power (4 W); one would expect that higher pressures will lead to higher power absorption and therefore to higher electron densities. The spatial distribution of the excited species was monitored using OES ( $2p$  states of Ar and Kr) and TLAS [Ar( $1s_5$ ) metastable state], and showed a plasma confined around the X-ray beam area for the pressure range between 50 and 500 mbar. The confinement region did not depend on the gas pressure (within the given range) or on the X-ray beam power, only on the size of the X-ray beam. This shows that diffusion of particles is limited by collisions to a distance smaller than the X-ray beam size (1–2 mm). The gas temperature in the central region is found to be from 400 to 1100 K, depending on the power and properties of the incident

X-ray beam. The increase in temperature leads to a decrease in gas density; as a consequence, the X-ray absorption cannot be simply calculated from the initial gas density. This is in agreement with previous studies on the X-ray absorption of gas attenuators, in which a density lower than the initial one was found.

The generation of plasma by the X-ray beam in the gas attenuator has been demonstrated, indicating that a large number of processes must be taken into account to fully explain the X-ray absorption by the gas. In particular, the energy transfer from the absorbed photons to the walls of the attenuator might happen not only by heat transfer but also by light emission from excited states and by diffusion of plasma species (electrons, ions and excited states). In this work we have shown that diffusion of particles is greatly limited in the given pressure range, and therefore the energy transfer may be reduced to heat conduction and light emission. These phenomena, together with a detailed balance of the ionization and recombination in the plasma volume, should be taken into account in any theoretical model of a gas attenuator. The data presented in this paper could also be used to validate such a model.

## Acknowledgements

We acknowledge the Réseau Plasmas Froids of the CNRS for the use of the tunable laser diode setup. We would also like to thank the staff of the ID06 beamline, Carsten Detlefs and Pierre Watechamps, for their assistance during the performance of the experiment, and Manuel Sánchez del Río for useful discussions. Finally we thank the ESRF for the beam time used for the experiments.

## References

- Aleksandrov, N. L. (2005). *Plasma Phys. Rep.* **31**, 425.
- Allen, J. E., Boyd, R. L. F. & Reynolds, P. (1957). *Proc. Phys. Soc. B*, **70**, 297–304.
- Álvarez, R., Rodero, A. & Quintero, M. (2002). *At. Spectrosc.* **57**, 1665–1680.
- Aragón, C. & Aguilera, J. A. (2008). *At. Spectrosc.* **63**, 893–916.
- Beckers, J., van der Horst, R. M., Osorio, E. A., Kroesen, G. M. W. & Banine, V. Y. (2016). *Plasma Sources Sci. Technol.* **25**, 035010.

- Belmonte, T., Noël, C., Gries, T., Martin, J. & Henrion, G. (2015). *Plasma Sources Sci. Technol.* **24**, 064003.
- Belostotskiy, S. G., Ouk, T., Donnelly, V. M., Economou, D. J. & Sadeghi, N. (2010). *J. Appl. Phys.* **107**, 053305.
- Belostotskiy, S. G., Ouk, T., Donnelly, V. M., Economou, D. J. & Sadeghi, N. (2011). *J. Phys. D*, **44**, 145202.
- Biasci, J.-C., Plan, B. & Zhang, L. (2002). *J. Synchrotron Rad.* **9**, 44–46.
- Carbone, E. A. D., Hübner, S., van der Mullen, J. J., Kroesen, G. M. W. & Sadeghi, N. (2013). *J. Phys. D*, **46**, 415202.
- Carbone, E., van Veldhuizen, E., Kroesen, G. & Sadeghi, N. (2015). *J. Phys. D*, **48**, 425201.
- Chavanne, J., Le Bec, G. & Penel, C. (2011). *Synchrotron Radiat. News*, **24**, 10–13.
- Chen, F. F. (2001). *Phys. Plasmas*, **8**, 3029–3041.
- Chubar, O. & Elleaume, P. (1998). *Proceedings of the Sixth European Particle Accelerator Conference (EPAC98)*, pp. 1177–1179. Bristol: Institute of Physics.
- Chumakov, A., Rüffer, R., Leupold, O., Celse, J.-P., Martel, K., Rossat, M. & Lee, W.-K. (2004). *J. Synchrotron Rad.* **11**, 132–141.
- Deline, C., Gilchrist, B., Dobson, C., Jones, J. & Chavers, D. (2007). *Rev. Sci. Instrum.* **78**, 113504.
- Elson, E. & Rokni, M. (1996). *J. Phys. D*, **29**, 716–725.
- Feng, Y., Krzywinski, J., Schafer, D. W., Ortiz, E., Rowen, M. & Raubenheimer, T. O. (2016). *J. Synchrotron Rad.* **23**, 21–28.
- Hernández, C. F. (2010). Master's thesis, ETSII Madrid, Spain; Grenoble INP, France.
- Hübner, S., Sadeghi, N., Carbone, E. A. D. & van der Mullen, J. J. A. M. (2013). *J. Appl. Phys.* **113**, 143306.
- Jonkers, J., van Dijk, J. & van der Mullen, J. A. M. (1999). *J. Phys. D*, **32**, 898–905.
- Konjević, N., Lesage, A., Fuhr, J. R. & Wiese, W. L. (2002). *J. Phys. Chem. Ref. Data*, **31**, 819–927.
- Latrasse, L., Sadeghi, N., Lacoste, A., Bès, A. & Pelletier, J. (2007). *J. Phys. D*, **40**, 5177–5186.
- Leiweke, R. J. & Ganguly, B. N. (2013). *J. Appl. Phys.* **113**, 143302.
- LXCat (2015). *Biagi-v8.9 database*, <http://www.lxcat.net>. Retrieved 1 July 2015.
- Palomares, J., Iordanova, E., van Veldhuizen, E., Baede, L., Gamero, A., Sola, A. & van der Mullen, J. (2010). *At. Spectrosc.* **65**, 225–233.
- Peterson, E. & Talbot, L. (1970). *AIAA J.* **8**, 2215–2219.
- Petrov, G. M. & Ferreira, C. M. (1999). *Phys. Rev. E*, **59**, 3571–3582.
- Pretzier, G. (1991). *Z. Naturforsch. A*, **46**, 639–641.
- Regt, J. M. de, Tas, R. D. & van der Mullen, J. A. M. (1996). *J. Phys. D*, **29**, 2404–2412.
- Requardt, H., Renier, M., Brochard, T., Bräuer-Krisch, E., Bravin, A. & Suortti, P. (2013). *J. Phys. Conf. Ser.* **425**, 022002.
- Rousseau, A., Teboul, E. & Béchu, S. (2005). *J. Appl. Phys.* **98**, 083306.
- Ryutov, D. D., Bionta, R. M., Kishiyama, K. I., McMahon, D., Roeben, M. D., Shen, S. & Stefan, P. M. (2009). *The Physics of the Gas Attenuator for the Linac Coherent Light Source*. Technical Report LCLS-TN-09-5. Linac Coherent Light Source, SLAC National Accelerator Laboratory, Menlo Park, CA, USA.
- Sadeghi, N. (2004). *J. Plasma Fusion Res.* **80**, 767–776.
- Sáinz, A., Díaz, A., Casas, D., Pineda, M., Cubillo, F. & Calzada, M. D. (2006). *Appl. Spectrosc.* **60**, 229–236.
- Saloman, E., Hubbell, J. & Scofield, J. (1988). *At. Data Nucl. Data Tables*, **38**, 1–196.
- Sudit, I. D. & Woods, R. C. (1994). *J. Appl. Phys.* **76**, 4488–4498.
- Zhang, L., Sánchez del Río, M., Monaco, G., Detlefs, C., Roth, T., Chumakov, A. I. & Glatzel, P. (2013). *J. Synchrotron Rad.* **20**, 567–580.